Energy Storage Materials 42 (2021) 826–835

Contents lists available at ScienceDirect

Energy Storage Materials

journal homepage: www.elsevier.com/locate/ensm

A novel phosphonium ionic liquid electrolyte enabling high-voltage and high-energy positive electrode materials in lithium-metal batteries

Fanglin Wu[a,b], Annika Regitta Schür[a,b], Guk-Tae Kim[a,b,*], Xu Dong[a,b], Matthias Kuenzel[a,b], Thomas Diemant[a], Gina D'Orsi[c], Elisabetta Simonetti[c], Massimo De Francesco[c], Mariangela Bellusci[c], Giovanni Battista Appetecchi[c,*], Stefano Passerini[a,b,*]

[a] Helmholtz Institute Ulm (HIU), Helmholtzstrasse 11, 89081 Ulm, Germany
[b] Karlsruhe Institute of Technology (KIT), P.O. Box 3640, 76021 Karlsruhe, Germany
[c] ENEA, SSPT-PROMAS-MATPRO Technical Unit, Via Anguillarese 301, 00123 Rome, Italy

ARTICLE INFO

Keywords:
Phosphonium cation
Ionic liquid
Electrolyte
$Li_{1.2}Ni_{0.2}Mn_{0.6}O_2$
High-voltage lithium-metal battery

ABSTRACT

The synthesis of a new ionic liquid (IL), consisting of the symmetric tetra-butyl-phosphonium (P_{4444}^+) cation and the (nonafluorobutanesulfonyl)(trifluoromethanesulfonyl)imide (IM_{14}^-) anion, via a facile and environmentally-friendly aqueous route is reported. The novel $P_{4444}IM_{14}$ IL demonstrates excellent thermal and electrochemical stability (beyond 6 V vs. Li^+/Li^0 (against Ni-foil)) in combination with good near-room temperature conductivity and ionic liquid characteristics, such as non-measurable volatility and exceptional flame-retardant properties. Employed as electrolyte component in Li-metal cells together with the high-voltage, $Li_{1.2}Ni_{0.2}Mn_{0.6}O_2$ positive electrode material, enables an initial discharge capacity of 264 mA h g^{-1} at 12.5 mA g^{-1} and improved initial Coulombic efficiency. Additionally, the discharge capacity retention is promising (92.3% after 50 cycles and 84.4% after 100 cycles) when compared with using a conventional organic carbonate-based electrolyte (55.5% after 50 cycles). Further development of this ionic liquid electrolyte may facilitate the practical application of Li-metal anodes in high-voltage/high-energy lithium batteries.

1. Introduction

Exploiting high-energy density lithium-metal batteries has become the ultimate goal of lithium-ion battery development to meet the ever increasing demand for extended driving ranges of electric vehicles (EVs) [1]. Among the various negative electrode (anode) materials, lithium metal is considered the most promising candidate because of its high specific capacity (3,860 mA h g^{-1}) and the lowest negative electrochemical potential (-3.04 V vs. the H^+/H_2 redox couple) [2,3]. However, Li-metal batteries face severe safety issues associated with the formation of Li dendrites and cavities, i.e., the occurrence of non-uniform Li deposition and stripping, respectively [4]. These phenomena may eventually lead to short circuit of the cell, promoting thermal runaway with the risk of explosion and/or fire when highly flammable conventional organic electrolytes are used [5]. As a result, the commercialisation of rechargeable Li-metal batteries has been largely limited thus far.

To overcome these challenges, an electrolyte featuring non-flammability due to low-volatility would be a crucial step towards the implementation of Li-metal battery systems [6,7]. Ionic liquids (ILs) represent an appealing alternative to replace the hazardous, conventional organic carbonate solvents in the electrolyte. Moreover, ILs often display a much broader electrochemical stability window (ESW) compared to conventional organic carbonate-based electrolytes,[8] which usually start to decompose (oxidation) above ~4.5 V at 25°C and ~4.3 V at 60°C [9]. As the ESW is a key factor for applications with high-voltage cathode systems, the safer and more stable ILs appear to be an attractive substitute. Among the most investigated ILs for electrochemical energy storage devices, those based on quaternary ammonium and imidazolium cations, in combination with per(fluoroalkanesulfonyl)imide anions, are the most relevant [10-13]. Nevertheless, during the last years ILs containing the phosphonium cation were successfully introduced [14-16]. These phosphonium-based ILs display higher thermal stability and wider electrochemical window compared with those employing quaternary ammonium cations, and sometimes, depending on the cation and/or anion structure, also offering lower viscosities and glass transition temperatures [17,18]. In addition, the interface between phosphonium-based electrolytes and Li-metal anode has been investigated by Howlett et al. [19] demonstrating that a more uniform solid electrolyte interphase (SEI) tends to form on the Li-metal surface using high concentrations of the lithium salt, while the main components

* Corresponding authors.
E-mail addresses: guk-tae.kim@kit.edu (G.-T. Kim), gianni.appetecchi@enea.it (G.B. Appetecchi), stefano.passerini@kit.edu (S. Passerini).

https://doi.org/10.1016/j.ensm.2021.08.030
Received 26 January 2021; Received in revised form 20 August 2021; Accepted 22 August 2021
Available online 25 August 2021

of the SEI layer are lithium fluoride (LiF) and decomposition products of lithium sulfide (Li_2S) [20]. Furthermore, the effect of the cation structures on the local ion arrangement and transport have also been explored for the phosphonium-based ILs indicating that larger sized cations tend to aggregate with more lithium ions [18]. Nevertheless, although these ILs possess relatively wide ESWs [6,21,22], generally, they are not sufficiently broad to allow applications with high-voltage cathodes requiring charge voltages above 4.8 V, such as Li-rich layered oxides ($Li_{1+x}M_{1-x}O_2$, M = Mn, Ni, Co, etc.) [23], Li spinel oxides ($LiNi_{0.5}Mn_{1.5}O_4$) [24], and some polyanionic compounds [25]. Therefore, it is imperative to develop a more electrochemically and thermally stable electrolyte for high-voltage lithium metal batteries.

Based on this, a novel ionic liquid, consisting of the symmetric tetra-butyl-phosphonium (P_{4444}^+) cation and the asymmetric (nonafluorobutanesulfonyl)(trifluoromethanesulfonyl)imide (IM_{14}^-) anion was designed and prepared via a simple environmental-friendly aqueous route. This peculiar scheme differs from the established concept choosing an asymmetric cation which favorably influences the physicochemical properties of the IL to a great extent, such as lowering the melting point and improving ion transport properties [14]. However, herein, the highly symmetric large P_{4444} cation was chosen due to its excellent structural stability that is expected to dramatically enhance the electrochemical and thermal stability of the ionic liquid. Subsequently, several different anions of the per(fluoroalkanesulfonyl)imide family with differing steric hindrance were selected to combine with the P_{4444} cation, namely P_{4444}FSI, P_{4444}TFSI and P_{4444}BETI. The $P_{4444}IM_{14}$ ionic liquid displays superior properties well beyond the series of comparison as summarized by the detailed physicochemical characterization.

Finally, $P_{4444}IM_{14}$ was employed in combination with lithium bis(trifluoromethanesulfonyl)imide (LiTFSI) as electrolyte salt for high-energy Li-metal cells using the Co-free $Li_{1.2}Ni_{0.2}Mn_{0.6}O_2$ (LRNM) positive electrode (cathode) material, and achieving outstanding electrochemical performance under high-voltage and high temperature conditions. This is even more remarkable considering this lithium-rich layered oxide offers high capacities but faces severe structural degradation and poor thermal stability in common organic carbonate-based electrolytes [26].

2. Experimental Section

2.1. Materials synthesis

P_{4444}FSI, P_{4444}TFSI, P_{4444}BETI and $P_{4444}IM_{14}$ were synthesised through an eco-friendly procedure which is described in detail elsewhere [27] using only deionised water as the processing solvent. The chemicals, i.e., tetrabutylphosphonium bromide (P_{4444}Br, Sigma-Aldrich, 98 %), activated carbon (charcoal, Sigma-Aldrich) and aluminum oxide (acidic, Sigma-Aldrich), were purified through a route previously reported [28], whereas sodium bis(fluorosulfonyl)imide (NaFSI, > 99.9 %, Solvionic), lithium bis(trifluoromethanesulfonyl)imide (LiTFSI, > 99.9 %, 3M), lithium bis(pentafluoroethanesulfonyl)imide (LiBETI, > 99.9 %, 3M) and (nonafluorobutanesulfonyl)(trifluoromethanesulfonyl)imide acid (HIM_{14}, 60 wt.% in water solution, 3M) were used as received. The deionised water was provided by a Millipore ion-exchange resin deioniser. All ILs and electrolytes were handled in a controlled atmosphere dry-room and vacuum-dried in a Büchi oven coupled with a turbomolecular pump ($<10^{-7}$ mbar) at 110°C for 24 hours.

The $0.8P_{4444}IM_{14}$-0.2LiTFSI electrolyte (PIM) was prepared by mixing the exact amounts of IL and lithium salt in a molar ratio equal to 4:1 (corresponding to a LiTFSI molar concentration of ca. 0.45M). The two components, handled in the dry-room, were stirred at 50°C until the LiTFSI was fully dissolved. The $Li_{1.2}Ni_{0.2}Mn_{0.6}O_2$ material was synthesized via a solid state reaction based on the transition metal sulfate sources [23].

2.2. Materials characterisation

The purity content of the IL samples was investigated by UV-Vis spectrophotometry (Shimadzu mod. 1800 UV-Vis spectrometer) in the 190-1100 nm wavelength range at room temperature. X-ray fluorescence spectrometry (EDX-720 Shimadzu spectrometer) was used to determine the halide content. The measurements were carried out according to a route described elsewhere [28]. The moisture content was measured through standard Karl Fischer titrations performed in a dry room by an automatic Karl Fischer coulometer titrator (Mettler Toledo DL32) at 20°C.

The thermal properties were determined by differential thermal (DTA) and thermo-gravimetric (TGA) analyses. The investigated samples (3-4 mg) were housed in alumina crucibles. Prior to each measurement, the instrument (Perkin Elmer Pyris Diamond TGA/DTA) was calibrated with the weight of the empty crucible (subsequently loaded with the sample, which was weighed by means of an external balance). The DTA measurements were carried out in argon atmosphere by running a heating scan (10°C min^{-1}) from room temperature (or -5°C) up to 150°C. Isothermal TGA measurements were performed to study the thermal stability of the phosphonium-based ILs during prolonged periods of heating. The IL samples, introduced into the calorimeter at room temperature, were subjected to successive heating periods (each one lasting 3 hours). The flash point of selected electrolytes was measured with a Miniflash FLPH instrument (Grabner).

The ion transport properties were investigated by examining the ionic conductivity as a function of the temperature. The IL samples (handled inside the dry room) were if necessary liquefied and transferred in sealed glass cells (AMEL 192/K) equipped with two porous platinum electrodes. The cell constant values were determined by measuring KCl aqueous solutions of known specific conductivity. Subsequently, the cells were placed inside the climatic chamber and kept at 0°C for 24 hours. Conductivity measurements (AMEL 160 conductivity meter) were carried out in the 0 - 125°C temperature range using a climatic chamber (Binder MK53) by performing a heating scan at 1.5°C h^{-1}, the conductivity values were recorded at temperature intervals of 5°C.

Powder x-ray diffraction (XRD) characterisation of LRNM electrodes was performed using a Bruker D8 Advance diffractometer (Cu K_α radiation, λ = 0.154 nm) in a 2θ range of 10-90°. Rietveld refinement was carried out using Topas software. A Chebyshev type background was fitted. A Thompson-Cox-Hastings (THC) peak type was applied for the instrumental resolution function. The Al foil was fitted with a preferred orientation in the (022) plane.

For x-ray photoelectron spectroscopy (XPS) measurements, LRNM electrodes were subjected to one full charge-discharge cycle, then very carefully washed with anhydrous DMC solvent to remove the electrolyte (LP30 or PIM) and transferred into the spectrometer under inert gas atmosphere. Spectra were acquired on the samples as such and after sputtering with Ar-ions for 30 minutes (~0.1 nm min^{-1} sputter rate, 20 nA, 5 kV) to gain insight into the cathode-electrolyte interphase (CEI) layer depth composition. The measurements were carried out on a Specs XPS system with a Phoibos 150 energy analyser using monochromatic Al K_α radiation (1486.6 eV), a take-off angle of 45° and pass energies of 30 and 90 eV at the analyser for detail and survey spectra, respectively. The peak fitting of the data was performed with CasaXPS, using Shirley-type backgrounds and Gaussian-Lorentzian peak shapes. For the p peaks (P2p and S2p), peak doublets with the expected intensity ratio (2:1) and spin-orbit splitting(s) were used for the peak fitting. All spectra were calibrated to the C (1s) peak of adventitious C (C-C/C-H species) at 284.8 eV.

2.3. Electrochemical measurements

The electrochemical stability of the $0.8P_{4444}IM_{14}$-0.2LiTFSI electrolyte was evaluated by liner sweep anodic voltammetry (Solartron 1260) using Pt, Ni and carbon (Super C65, Imerys, supported on Al foils) working electrodes (WEs), and Li metal as counter electrode. The cell

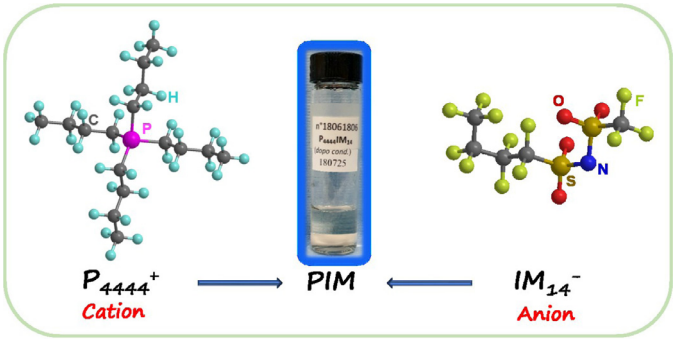

Fig. 1. Structure of the P_{4444}^{+} cation and the IM_{14}^{-} anion.

voltage was swept (0.1 mV s^{-1} scan rate) from the open circuit value (OCV) towards more positive (anodic) or negative (cathodic) voltages. The anodic and cathodic cyclic voltammetry (CVs) values were recorded using WEs consisting of carbon deposited Al and Cu foils, respectively. Stripping/plating tests (Maccor battery tester 4300) were performed on symmetrical Li/Li cells, which were subjected to galvanostatic (*0.1 mA cm^{-2}, 0.05 mA cm^{-2}*) charge/discharge cycles (each one lasting 1 hour).

Li/LRNM pouch cells were assembled (see photographs in **Fig. S1**) to compare the performance of $0.8P_{4444}IM_{14}$-0.2LiTFSI with that of commercial LP30. The LRNM cathode was prepared by mixing the active material, the conductive agent (carbon Super C65, IMERYS) and the binder (polyvinylidene difluoride, PVdF, Solef 6020, Arkema) in a weight ratio of 85:10:5. The slurry, prepared using *N*-methyl-2-pyrrolidone (NMP; anhydrous, > 99.5%; Sigma-Aldrich) as the dispersant medium, was cast onto aluminum foil (20 μm). A lithium sheet was used as the anode (width: 2 cm, thickness: 0.5 mm, Rockwood Lithium, battery grade). After drying at 80°C overnight, the electrodes were punched into 12 mm diameter disks and vacuum dried at 120°C for 12 h. The average mass loading was 2 ± 0.2 mg cm^{-2}. The Li/LRNM cells were charged up to a cut-off voltage of 4.8 V for activation at 0.05 C current rate during the first two cycles, then cycled between 2.5 - 4.8 V at 0.1 C. All voltage values are referred to the Li^{+}/Li^{0} redox couple. A (dis)charge rate of 1 C corresponds to a specific current of 250 mA g^{-1}.

The $0.8P_{4444}IM_{14}$-0.2LiTFSI and LP30 electrolyte were supported (within the cells) by Whatman glass fibre GF/A separators (~100 μL). All electrochemical cells except those for LSV measurements with a Pt working electrode (here a Swagelok-type two-electrode cell was assembled in the glove box), were assembled in the dry room and housed in vacuum-sealed soft envelopes according to the description in **Fig. S1**. The general electrochemical measurements were performed in climatic chambers at 40 (± 2) °C, a variable temperature electrochemical measurement was also performed at 60 (± 2) °C and 80 (± 2) °C.

3. Results and Discussion

The (P_{4444}^{+})-based ILs purities were found to be higher than 99.9 % as determined according to the analytical procedure reported in the literature [28]. In particular, the content of lithium, halide and moisture is below 2 ppm. Apart from $P_{4444}IM_{14}$ (Fig. 1), all investigated (P_{4444}^{+}) ILs are solid at room temperature.

3.1. Comparison of physical properties of P_{4444}^{+}-based ionic liquids

The DTA (panel a) and isothermal TGA (panel b) results are illustrated in Fig. 2. Below the melting temperature, P_{4444}FSI and P_{4444}TFSI show a well-defined endothermic feature (Fig. 2**a**, highlighted with the * symbol), located around 83°C and 70°C, respectively. This feature, already observed in other ILs, is ascribable to a solid-solid phase transition (which occurs before the melting) resulting from the change of the ILs crystalline structure [14,29]. A second, well-evident endothermic peak (Fig. 2**a**) observed at 97°C for P_{4444}FSI and 85°C for P_{4444}TFSI (Table 1), is associated to the melting of the two ILs. Conversely, the thermograms of P_{4444}BETI (Fig. 2**a**) and $P_{4444}IM_{14}$ (Fig. 2**b**) show only one endothermic feature related to the melting, located at 116°C and 24°C, respectively (Table 1). The absence of the endothermic feature (*) is presumably due to the kinetic effects (related to solid-solid transitions) exhibited by these IL materials [30-33], which can be attributed to the greater steric hindrance of the $BETI^{-}$ and IM_{14}^{-} anions, compared to the FSI^{-} and $TFSI^{-}$ ones. In the case of IM_{14}^{-}, its very high asymmetry (which hampers the structural reorganisation of the ions within the IL sample) additionally contributes to this effect and significantly lowers the melting point close to room temperature. Therefore, eventual solid-solid phase transitions are not visible in the P_{4444}BETI, and $P_{4444}IM_{14}$ samples as the DTA measurements are carried out at a relatively high scanning rate (10°C min^{-1}). Finally, the weak feature in the $P_{4444}IM_{14}$ sample located between 8 and 10°C in the measurement of $P_{4444}IM_{14}$ (Fig. 2**b**) is caused by the calorimeter (i.e., not related to any phase transition). The much lower melting temperature of $P_{4444}IM_{14}$ is certainly bound to the asymmetry of the anion (IM_{14}^{-}), which hinders the structural organisation of the ions.

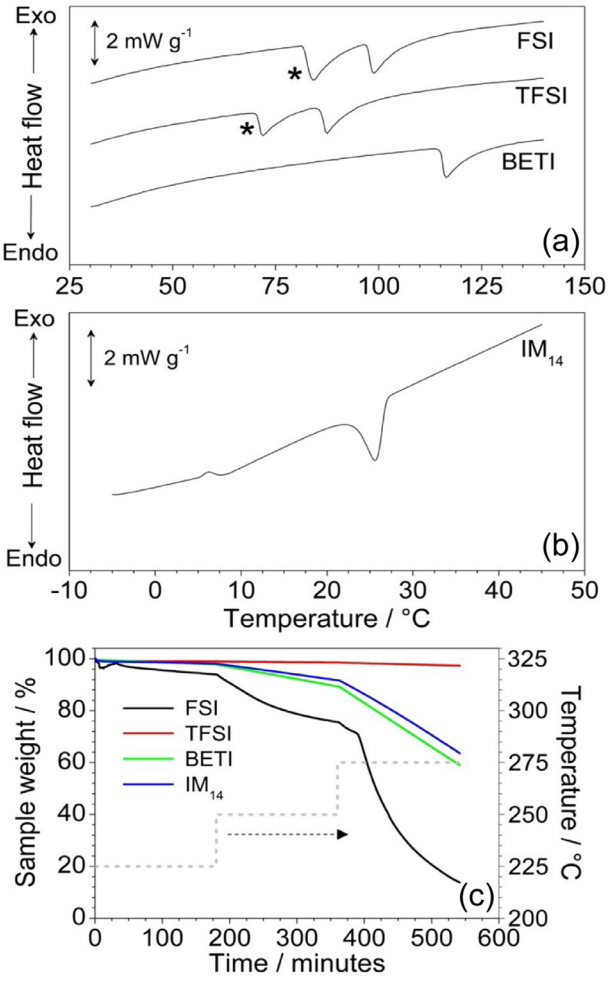

Fig. 2. DTA a) and b) and isothermal TGA, c) traces of different (P_{4444}^{+}) ILs. Scan rate (DTA): 10°C min^{-1}. The temperature vs. time profile (TGA) is represented by the stepwise grey trace. The weak feature observed for $P_{4444}IM_{14}$ in panel b between 8 and 10°C is an instrumental artefact.

With the exception of $P_{4444}IM_{14}$, the ILs exhibit melting above room temperature. (Table 1). Conversely, the $P_{4444}IM_{14}$ sample (Fig. 2**b**) displays a near-room temperature melting point (24°C), due to the high asymmetry and steric footprint of the IM_{14}^{-} anion, which hampers the formation of the crystal lattice (i.e., the regular packing of the ions)

Table 1
Summary of the physicochemical properties of the tetra-butyl-phosphonium ionic liquids. T_m = melting temperature. T_d = thermal decomposition temperature.

IL sample	T_m /°C	T_d /°C	Ionic conductivity / S cm^{-1}	
			30°C	120°C
P_{4444}FSI	97.2 ± 0.5	< 200	(7.8 ± 0.8) × 10^{-8}	(1.1 ± 0.2) × 10^{-2}
P_{4444}TFSI	85.7 ± 0.5	275	(2.7 ± 0.3) × 10^{-7}	(8.4 ± 0.9) × 10^{-3}
P_{4444}BETI	116.4 ± 0.5	225	(2.2 ± 0.3) × 10^{-7}	(5.9 ± 0.6) × 10^{-3}
$P_{4444}IM_{14}$	24.3 ± 0.5	225	(1.7 ± 0.2) × 10^{-4}	(4.5 ± 0.5) × 10^{-3}

[29,31,34]. Similar behaviour has been previously observed in a few IM_{14}-based ILs including pyrrolidinium, imidazolium and tetraalkylammonium cations [29,31].

The thermal stability of the ILs has been studied via isothermal TGA experiments. The resulting traces (**Fig. 2c**) reveal a different behaviour among the four ILs. P_{4444}FSI shows a weight loss above 200°C (with rapid degradation at higher temperatures) whereas P_{4444}BETI and $P_{4444}IM_{14}$ are thermally stable up to 225°C (**Table 1**). This result confirms the already reported lower stability of FSI^- with respect to other per(fluoroalkanesulfonyl)imide anions [30,31]. However, the P_{4444}^+ ILs exhibits improved thermal stability than several other IL materials with similar anions as those in the present study, but different cations [30-32,34], confirming the greater stability of the P_{4444}^+ cation. Furthermore, a generic dependence on the steric dimensions of the anion is observed, in particular following the length of the fluorinated chain, with the exception of P_{4444}TFSI, which shows surprisingly negligible weight loss up to 275°C (**Table 1**). Such a high thermal stability is rarely observed in other families of ILs, including those based on different phosphonium cations [18,35-37]. This may be due to the high stability of the S-CF_3 bond with respect to the S-F bond in FSI as well as the higher stability of the longer perfluoroalkyl chains (-C_2F_5 and -C_4F_9) making them better leaving groups. However, further investigations are needed to fully clarify this behaviour.

The ion transport properties of the ILs play a key role on their viability as electrolyte components. **Fig. 3a** compares the ionic conductivity of the neat ILs as a function of the temperature. The conductivity values, in the range around 10^{-8}-10^{-7} S cm^{-1} at 0°C (typical for ILs in the solid state) [29,31], are seen to progressively increase up to 10^{-6}-10^{-5} S cm^{-1} prior to the melting temperature. This behaviour suggests an increasing ionic mobility already in the solid phase [29,31], in good agreement with the DTA measurements (**Fig. 2a**) revealing solid-solid phase transitions in P_{4444}FSI and P_{4444}TFSI, but not for P_{4444}BETI and $P_{4444}IM_{14}$. However, it should be noted that the conductivity measurements were performed at a scan rate of 1.5°C h^{-1}, i.e., considerably lower than that of the DTA ones (10°C min^{-1}), disclosing rather slow processes which are not detected by the thermal measurements.

The melting of the four ILs is highlighted by the abrupt increase of ionic conductivity (about three orders of magnitude), which is once more in good agreement with the DTA measurements (**Fig. 2a**). Ionic conductivity values higher than 10^{-4} and even 10^{-3} S cm^{-1} are recorded for the four ILs in the molten state, i.e., similar to those of other ILs consisting of analogous anions and different cations (pyrrolidinium, imidazolium and tetraalkylammonium) of interest for applications in electrochemical devices [29,31]. The further temperature increase up to 120°C (**Table 1**) results in the progressive increase of conductivity up to 10^{-2} S cm^{-1} for P_{4444}FSI, i.e., reaching the values of conventional organic electrolytes which, however, cannot operate at such high temperatures because of their volatility [38]. The ionic conductivity of the four ILs in the liquid state progressively decreases upon increasing of the anion molecular weight (**Table 1**) in the order: FSI > TFSI > BETI > IM_{14}.

3.2. Electrochemical characterisation of 0.8$P_{4444}IM_{14}$-0.2LiTFSI

Among the four ILs investigated, $P_{4444}IM_{14}$ is the only liquid at room temperature. Therefore, it was studied as electrolyte component in combination with LiTFSI salt (IL: LiTFSI mole ratio = 4: 1) [39]. **Fig. 3b** compares the conductivity *vs.* temperature dependence of pristine $P_{4444}IM_{14}$ and the 0.8$P_{4444}IM_{14}$-0.2LiTFSI (PIM) mixture. The introduction of the high charge density Li^+ cation leads to the disruption of the already poor tendency of $P_{4444}IM_{14}$ to crystallise. Interestingly, the incorporation of LiTFSI lowers the melting temperature of the mixture by inhibiting the long-range ion packing [40]. This allows for a dramatic gain in conductivity, up to three orders of magnitude, at temperatures below 30°C (from 10^{-6} to 10^{-4} S cm^{-1} at 25°C and from 10^{-8} compared to 10^{-5} S cm^{-1} at 0°C). In fact, PIM exhibits a Vogel-Tamman-Fulcher (VTF) behaviour [7] down to 0°C (i.e., no conductivity jump is observed) in full agreement with the viscosity versus temperature trend (**Fig. S2** in the Supplementary data). On the other hand, the strong Li^+—IM_{14}^- interactions occurring in PIM result only in the very moderate decrease in conductivity above 25°C.

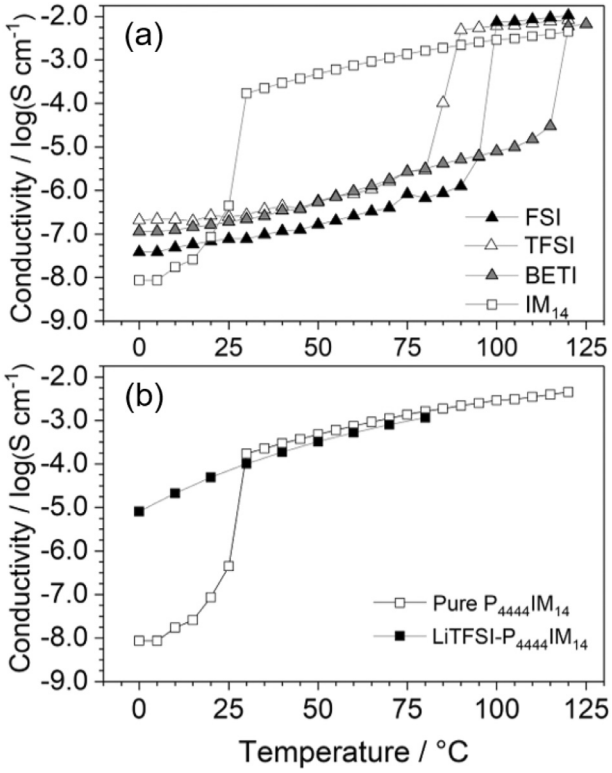

Fig. 3. Ionic conductivity vs. temperature dependence of: a) P_{4444}-based ionic liquids with different anions; b) pure $P_{4444}IM_{14}$ and 0.8$P_{4444}IM_{14}$-0.2LiTFSI (PIM) mixture. Scan rate: 1.5°C h^{-1}.

Besides good ionic conductivity, the ESW of the electrolyte is a critical property, especially in high operational voltage battery systems [21]. **Fig. 4** compares the anodic liner sweep voltammetry (LSV) curves for PIM obtained using carbon, platinum or nickel as the WE, manifesting low current flow up to about 5 V vs. Li^+/Li^0, 5.5 V vs. Li^+/Li^0 or beyond 6 V vs. Li^+/Li^0, respectively, before the steep current increase due to electrolyte decomposition occurs. The lower stability detected with

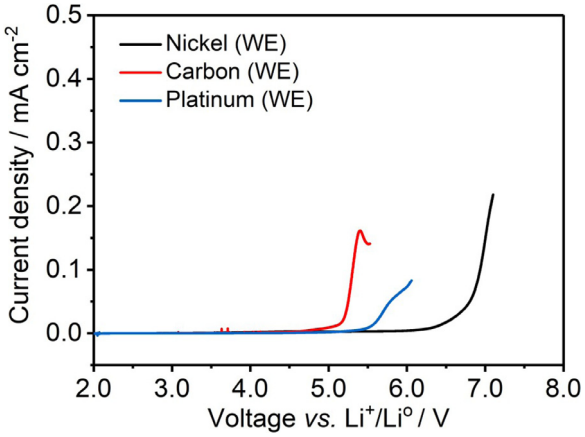

Fig. 4. Anodic sweep voltammetry of Li/0.8$P_{4444}IM_{14}$-0.2LiTFSI(PIM)/WE cells with different working electrodes (WEs). Scan rate: 0.1 mV s^{-1}. T = 40°C.

the carbon WE [40] is due to its larger surface area with reactive groups providing favourable sites for electrolyte decomposition, as well as for anion intercalation of electrolyte components into the graphitised carbon [41]. It is noteworthy that a low scan speed (0.1 mV s^{-1}) was used in order to effectively probe the robustness of the IL electrolyte towards oxidation. To the best of our knowledge, PIM shows higher anodic stability than most previously reported electrolytes, such as commercial organic battery electrolyte (4.5 V) [9], other phosphonium ILs [35,42]. This is due to the more stable quaternary phosphonium cation in comparison to the nitrogen-based ones. Furthermore, the PIM displays excellent flame-retardant properties (see corresponding flammability test supported in **Fig. S3**) and in contrast to a very low flash point for LP30 (~24 °C), no flash point could be detected at temperatures up to 300 °C, which is due to the extremely low vapour pressure of PIM [43].

PIM was also subjected to repeated anodic or cathodic cyclic voltage (CV) sweeps at 0.05 mV s^{-1} and 40°C, using carbon as WE (**Fig. S4**). The remarkable reduction of the anodic current flow from the first scan (about 1.5 μA cm^{-2} at 5.0 V, see panel (a) of **Fig. S4**) to the second and following CV cycles (below 0.25 μA cm^{-2}) strongly suggests that the irreversible oxidation process occurring during the first anodic sweep is associated with the impurities rather than the instability of the electrolyte's components [40]. On the cathodic side, repeated CVs (panel (b) in **Fig. S4**) clearly indicate the possibility of employing PIM for reversible lithium metal stripping/plating with good efficiency and without any visible electrolyte degradation. In fact, the observed current flow below 1.0 V vs. Li^+/Li^0 is extremely low (< 50 μA cm^{-2}) and related to the establishment of a thin SEI on the carbon electrode.

To highlight the compatibility of PIM towards the lithium metal anode, galvanostatic Li stripping/plating tests were carried out on symmetric Li/0.8$P_{4444}IM_{14}$-0.2LiTFSI (PIM)/Li cells at 40°C (**Fig. 5a**). A modest cell overvoltage value (< 50 mV) is observed after prolonged cycling (> 1,000 hours) at a constant current density of 0.05 mA cm^{-2}. This nearly unchanged overvoltage suggests sufficient Li^+ conductivity through the SEI film to enable reversible stripping plating on the lithium anode. However, when the current density is increased up to 0.1 mA cm^{-2}, the overvoltage displays a slow and steady rise until a sharp increase is observed after 400 h, indicating severe polarisation due to resistance build-up within the Li/Li cells. To provide further insight into the resistance build-up upon cycling, electrochemical impedance spectroscopy (EIS) measurements were performed. These measurements indicate a faster rise of the Li/electrolyte interfacial resistance (corresponding to the increasing diameter of the AC response in **Fig. 5b** and **c**) in the cell subjected to the stripping/plating test at 0.1 mA cm^{-2} in comparison to those performed at 0.05 mA cm^{-2}. Besides, the presence of the low frequency inclined straight-line (due to diffusion phenomena within the IL electrolyte) in the AC responses suggests that no short-circuit is occurring in the cells during the cycling tests.

3.3. Electrochemical performance comparison between LP30 and 0.8$P_{4444}IM_{14}$-0.2LiTFSI electrolyte

Finally, to evaluate the possible application of the novel electrolyte, PIM, with a lithium metal anode, cells were made in combination with the high-voltage and high-capacity LRNM cathode material. Their performance is compared with that of analogous Li/LRNM cells containing a conventional organic carbonate-based electrolyte (LP30, 1 M $LiPF_6$ in EC/DMC). **Fig. 6a** displays the first charge/discharge process of cells with LP30 and the IL-based electrolyte. During the first charge, an extended voltage plateau around 4.6 V is observed, which is related to the electrochemical activation of the Li_2MnO_3 phase involving anion redox activity and oxygen release occurring along the high voltage plateau [44]. However, both the electrolytes performed quite similarly during the first cycle. In fact, analogous voltage profiles and very similar discharge capacities are obtained for the PIM-based (264 mA h g^{-1}) and LP30-based (270 mA h g^{-1}) cells at 12.5 mA g^{-1} (0.05 C). The only difference is the slightly higher polarisation during charge observed in the cell employing PIM probably due to its slightly inferior ionic conductivity. This difference is highlighted by the differential capacity plots reported in **Fig. S5** for the LP30- and PIM-based cells, where the peak corresponding to the activation plateau is shifted to slightly higher potentials for the IL. However, the initial Coulombic efficiency in the 0.8$P_{4444}IM_{14}$-0.2LiTFSI electrolyte reaches 85.6 % compared with 83.4 % obtained with the organic carbonate-based electrolyte. The different performance offered by the two electrolytes is apparent upon long-term cycling tests (**Fig. 6b**) at 12.5 mA g^{-1} (first three cycles) and then 25.0 mA g^{-1} (0.1 C). At both current densities, the Li/0.8$P_{4444}IM_{14}$-0.2LiTFSI (PIM)/LRNM cells deliver nearly the same initial capacity (i.e., 270 mA h g^{-1} at 0.05 C and 250 mA h g^{-1} 0.1 C) as the ones employing LP30. However, the former cells show a much better capacity retention (i.e., 92.3 % vs. 55.5 % after 50 cycles) as well as higher Coulombic efficiency, indicating that PIM suffers less severe degradation phenomena than the standard electrolyte (LP30) at high operating voltages. Moreover, the capacity retention of 84.4% after 100 cycles in PIM is among the best, if not the best, reported for lithium-rich cathodes at elevated temperature (a comparison with previous studies is shown in **Table S1**). To investigate the high-voltage stability of PIM in a real cell, the effect of the upper cut-off voltage on the cell performance was evaluated (**Fig. 6c**). The results for the 1st full charge-discharge cycle show practically overlapping voltage vs. capacity curves during the first charge independently of the cut-off value (i.e., from 4.8 to 5.2 V). However, remarkable differences are seen in the discharge profiles, where the largest capacity (283 mA h g^{-1}) is obtained for the cut-off set at 5.0 V, while the cell charged up to 5.2 V shows lower discharge capacity. This performance degradation might be related to the IM_{14}^- anion intercalation into the conductive carbon, resulting in its degradation and, thus, increased cell polarisation [41,45], but also due to the structural degradation of the cathode material upon excess Li^+ extraction from the transition metal layer, resulting in the pronounced capacity fading observed upon cycling (see **Fig. S6**) [44,46]. Even so, it at least proves that PIM retains its good stability at high potentials (>4.8 V), in contrast to the cells employing LP30 (**Fig. S6**), which face severe electrolyte decomposition and cannot be repeatedly charged to 5.0 V or 5.2 V after the 1st cycle. In order to probe the effect of the operating temperature, the cells were also tested at an even higher temperature (60 °C, **Fig. S7**), which shows coinciding behaviour with the curve recorded at 40 °C during the first charge process, and an increased discharge capacity around 271 mA h g^{-1} that is likely attributed to the enhanced ionic conductivity of PIM at the higher operating temperature. However, this is accompanied by a slightly more pronounced loss of working voltage and capacity fading during the following cycles, which is typically observed for Li-rich layered oxides and caused by structural transformation associated to accelerated side reac-

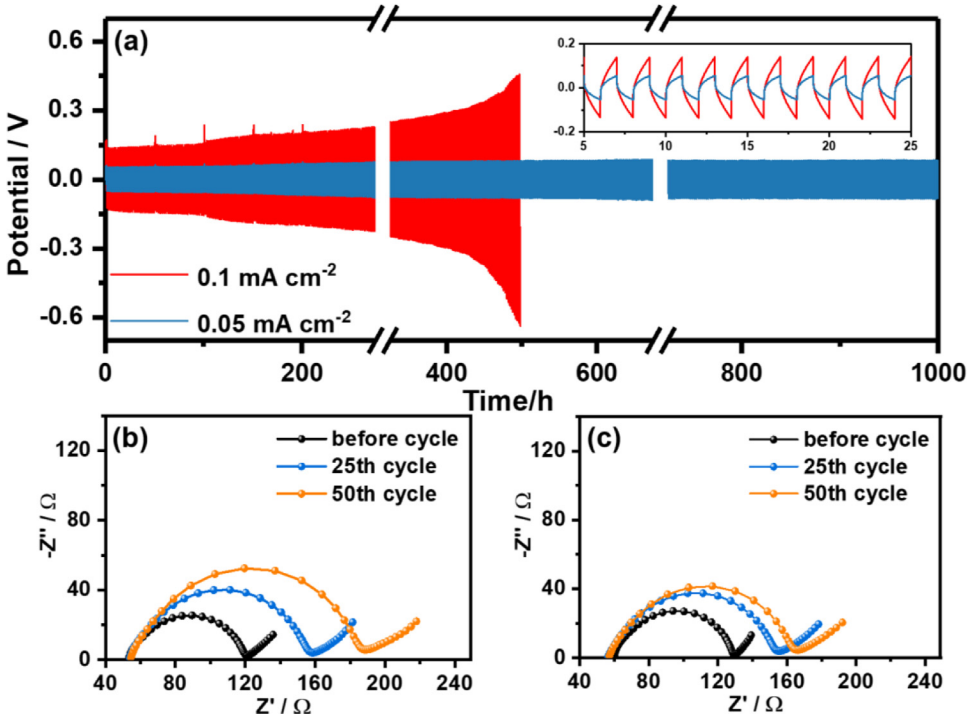

Fig. 5. a) overvoltage/time profiles during galvanostatic cycling (0.1 mA cm^{-2} and 0.05 mA cm^{-2}, with each stripping or plating step lasting for 1h. Time evolution of the AC responses for Li/0.8$P_{4444}IM_{14}$-0.2LiTFSI (PIM)/Li cells at b) 0.1 mA cm^{-2} and c) 0.05 mA cm^{-2}. All measurements were performed at T = 40°C.

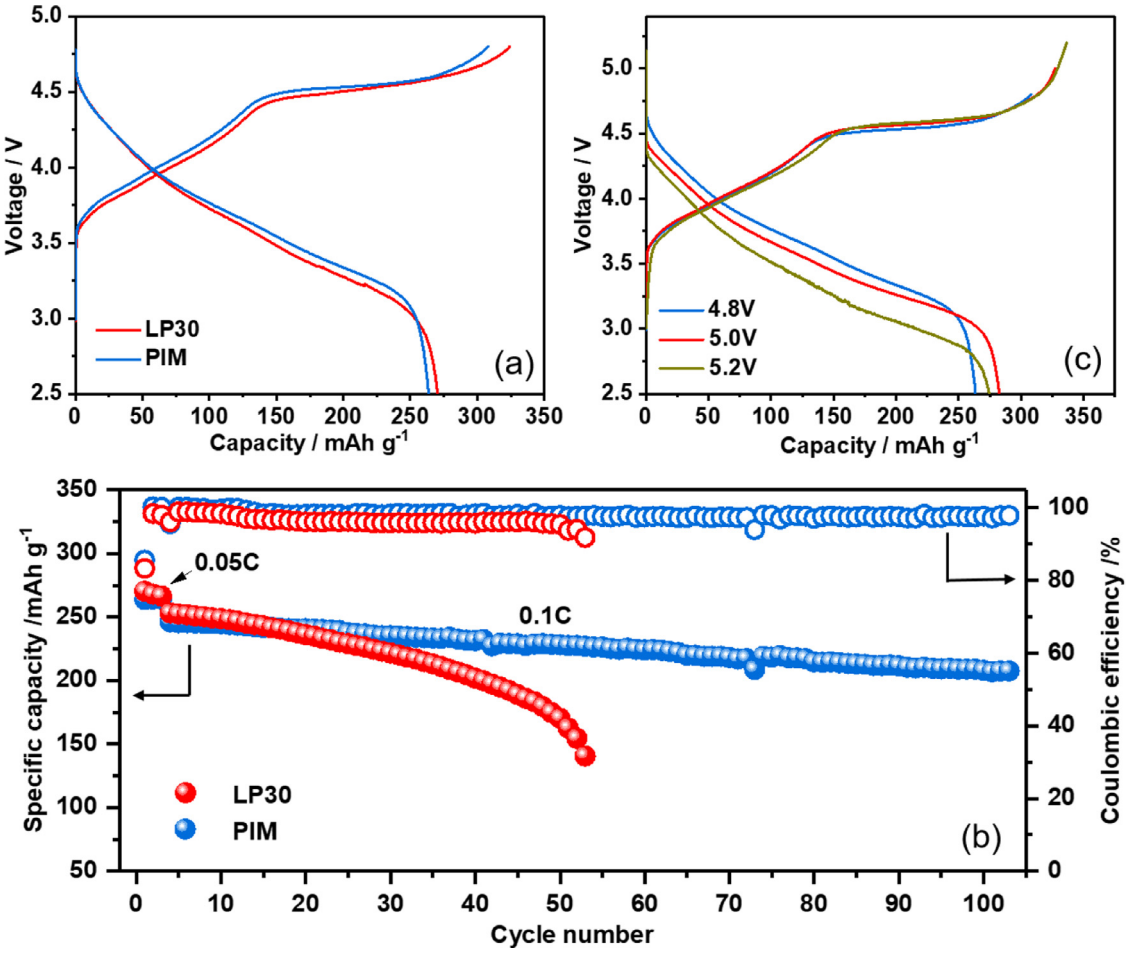

Fig. 6. a) Voltage vs. capacity (1st cycle) profiles and (b) long-term cycling performance of Li/LRNM cells employing the 0.8$P_{4444}IM_{14}$-0.2LiTFSI (PIM) and organic carbonate (LP30) electrolytes. c) Voltage vs. capacity profiles obtained for different cut-off voltages for Li/0.8$P_{4444}IM_{14}$-0.2LiTFSI (PIM)/LRNM cells during the first cycle. T = 40°C.

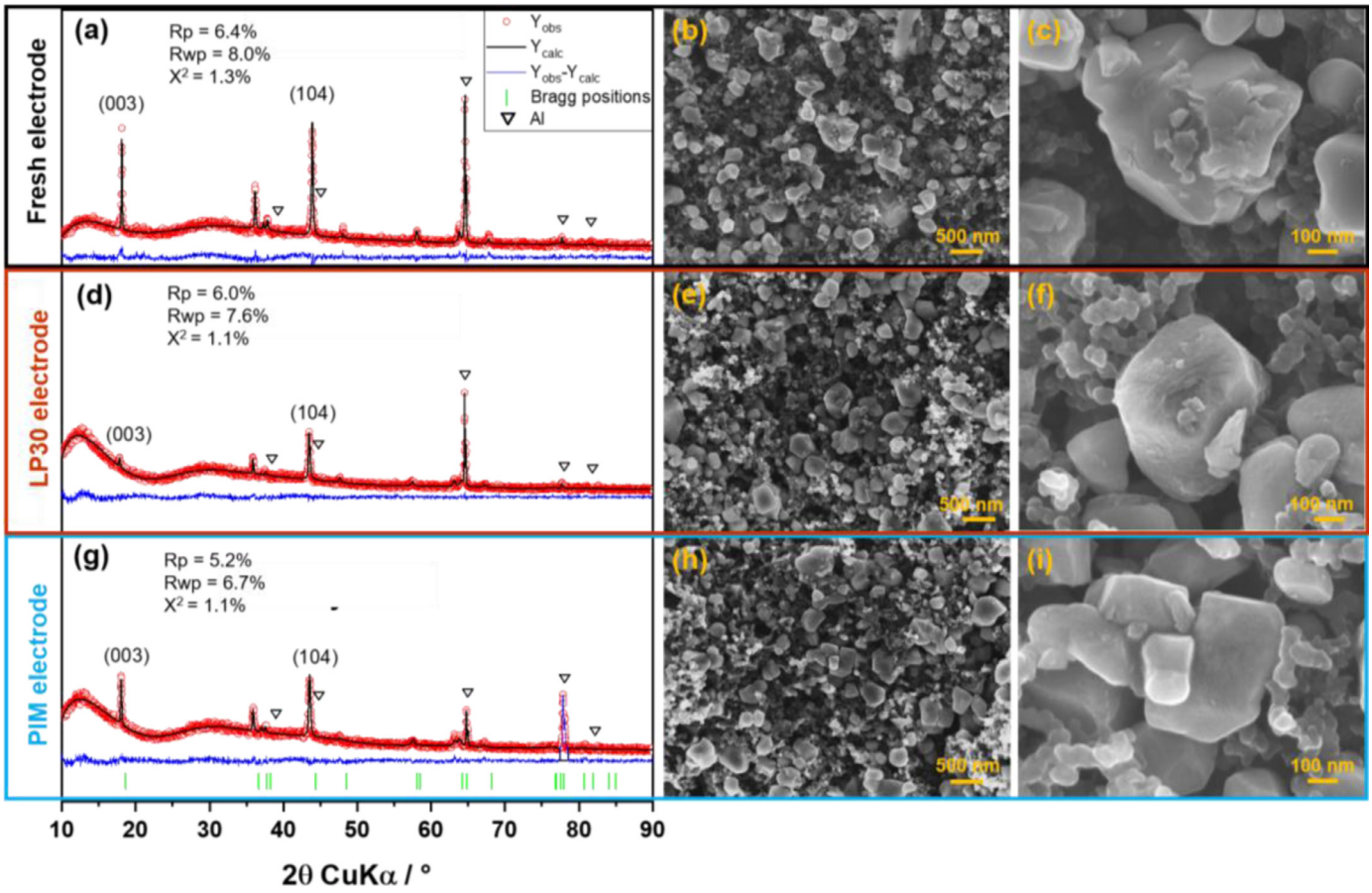

Fig. 7. XRD patterns and SEM micrographs of (a-c) fresh LRNM electrodes, and electrodes cycled in (d-f) LP30 (50 cycles) or (g-i) PIM ($0.8P_{4444}IM_{14}$-0.2LiTFSI, 100 cycles) electrolyte.

tions at the interphase as well as the tendency of aluminum corrosion at higher temperatures and operational voltages [47,48]. Even so, to affirm the excellent electrochemical and thermal stability of PIM, the cells were tested in conventional organic electrolyte (LP30), nitrogen-based ionic liquid electrolyte (which showed an excellent cycling stability with lithium-rich cathodes [49]) and PIM at an even higher temperature (80 °C, see **Fig. S8**). These tests revealed the superior cycling stability of the cell employing PIM, as well as the greatly improved rate capability.

3.4. Origin of improved electrochemical performance of $0.8P_{4444}IM_{14}$-0.2LiTFSI

In order to elucidate the origin of the enhanced electrochemical performance with the IL-based electrolyte, ex-situ XRD and scanning electron microscopy (SEM) measurements were performed on fresh electrodes as well as after 50 cycles in LP30 and 100 cycles in PIM, the results are presented in **Fig. 7**. In addition, XRD patterns of electrodes after one cycle in both electrolytes are displayed in **Fig. S9**. After the first cycle, there is no clear difference between the XRD patterns of both cycled electrodes and the fresh one (compare also refined atomic parameters summarised in **Tables S2 – S4**). However, after 50 cycles in LP30, the (003) reflection almost vanished. The intensity ratio of the (003) and (104) reflections decreases dramatically, which is correlated to the degree of cation mixing. This means that a higher degree of cation mixing, i.e., the occupation of Li^+ sites by migrating transition metal ions in the layered oxide cathode, occurs when the cathode material is cycled in LP30 [50]. In particular, a cation mixing degree of approximately 8% in LP30 (**Table S5**) is determined by Rietveld refinement. Upon cycling, Ni^{2+} ions occupy the Li^+ sites, gradually leading to the formation of a disordered rock-salt structure, which is one of the root causes for the capacity and voltage fading of Li-rich cathode materials [49,51]. In contrast, there is almost no cation mixing occurring in the electrode cycled (even for longer times) in the IL-based electrolyte (**Table S6**), explaining the superior cell performance upon extended cycling.

While SEM images with low magnification (20kx) do not show significant changes between the fresh and cycled electrodes (**Fig. 7b,e,h**), some differences could be identified in high magnification (100kx) images (**Fig. 7c,f,i**) and their enlargements (**Fig. S10**). First, while quite clean particle surfaces are seen in fresh electrodes, they become relatively rough in the cycled electrodes, especially when using LP30. This modification points to an apparent severe change of the surface morphology of the electrode particles in LP30. Second, the electrode particles cycled in LP30 show a more 'roundish' shape than the pristine ones. On the other hand, the electrode particles cycled in PIM remain mostly unchanged. In accordance with the XRD results, this suggests a gradual degradation during cycling in LP30, while a relatively stable and thin cathode interphase layer is formed in PIM electrolyte.

In the next step, XPS was used to detect the chemical components on the materials surface [52]. In particular, XPS measurements were performed to investigate the composition of the CEI formed on the LRNM particle surface derived from PIM in comparison to LP30 after the 1st electrochemical cycle (**Fig. S11**) and after prolonged cycling (**Fig. 8**). For the analysis of the electrodes after the initial cycle (**Fig. S11**), we focus our discussion mainly on the detail spectra in the F1s peak region, since F-containing species are key components of the CEI films grown on LRNM cathodes derived from LP30 (a) and PIM (b). Furthermore, spectra were recorded before (top) and after (bottom) sputtering with Ar^+ to obtain more insight into the depth distribution of the CEI species. The

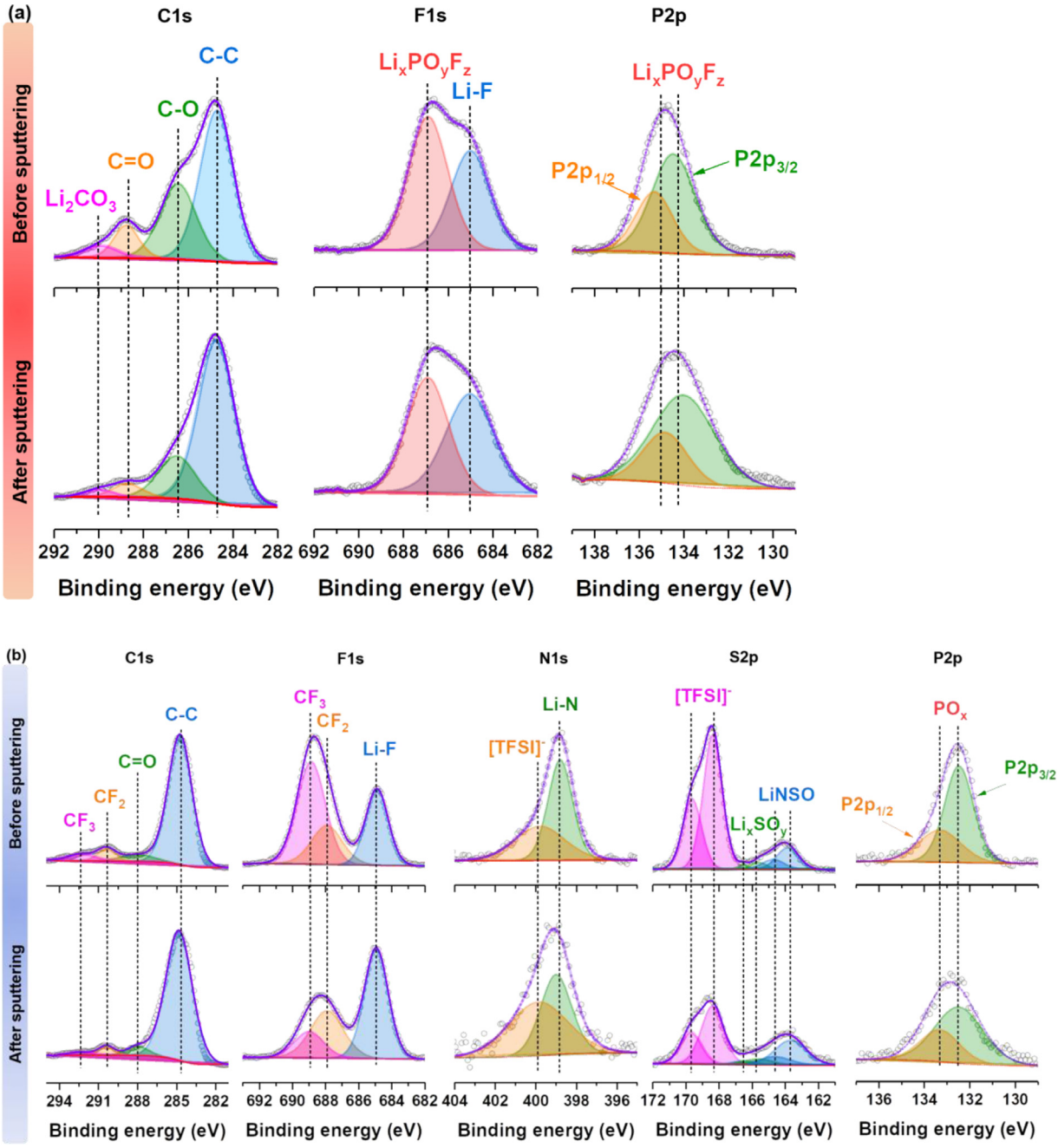

Fig. 8. XPS analysis of LRNM electrodes (a) after 50 cycles in LP30 and (b) after 100 cycles in PIM electrolyte recorded before (top) and after (bottom) Ar^+-sputtering. T = 40°C.

peak at 687.8 eV, which is evident in the spectra of both electrodes, is attributed to the CF_2 groups of the electrode binder (PVdF). A possible contribution from PF_6^- (or decomposition products of it, i.e., $Li_xPO_yF_z$) can be excluded for this sample due to the lack of corresponding features in the P2p detail spectra. The spectra of the PIM electrode show another peak at a higher binding energy (689.2 eV, panels b), which can be ascribed to the perfluorinated alkyl chains of PIM. Furthermore, the peak of LiF is detected at 685.0 eV. LiF is a key component of the CEI layer, which is typically formed from highly reactive HF which in turn is generated upon $LiPF_6$ decomposition by means of self-catalytic hydrolysis with trace levels of moisture [49,53,54]. The feature is evident in the spectra of both electrodes and is seen to remarkably increase upon sputtering, i.e., going closer to the LRNM surface. However, a much weaker LiF peak is observed for PIM, suggesting a lower amount of HF if any is generated in this electrolyte with the absence of reactive and unstable $LiPF_6$ salt. To confirm the extent of electrolyte decomposition, XPS measurements were also collected on electrodes after prolonged cycling (Fig. 8). For the electrode cycled in LP30 (Fig. 8**a**), the presence of $Li_xPO_yF_z$ species in the surface layer becomes evident by the detection of the corresponding peak features in the P2p (~134.5 eV) and F1s (686.9 eV) detail spectra. Furthermore, the F1s spectra show the LiF peak (685.0 eV) again. In addition, the C1s spectra display the features of C-O and C=O groups and Li_2CO_3 at 286.5 eV, 288.7 eV, 290.0 eV, respectively, which can be assigned to the decomposition products of the electrolyte's solvents. Taken together, these results verify the extensive decomposition of LP30 upon prolonged cycling, also leading to the presence of HF intermediates and the formation of by-products such as $Li_xPO_yF_z$, LiF among others [49,55]. While certain decomposition prod-

ucts are beneficial and important components for the build-up of the CEI layer, a continuously thickened CEI layer will adversely affect the Li^+ transport kinetics [51,56]. From the comparison of Mn2p spectra intensity after the 1st cycle and prolonged cycling in both electrolytes (**Fig. S12**), the intensity of Mn2p in the electrode cycled in LP30 is obviously weaker than that cycled in PIM, indicating a thicker CEI layer forms in the presence of LP30. More importantly, the HF, which is formed during electrolyte decomposition, will attack the cathode surface and exacerbates the cation mixing in the active electrode material, eventually resulting in the formation of the undesired rock-salt phase [51]. In contrast, there is no evidence of HF formation by hydrolysis in the PIM electrolyte. For the electrodes cycled for one cycle in PIM, the XPS measurements show the presence of undecomposed ionic liquid and LiTFSI (full removal of these products is difficult to achieve). Also, a small amount of decomposition products of the electrolyte is detected, e.g., in the S2p detail spectra (Li_xSO_y, LiNSO), which are characteristic of the $IM14^-$ anion and lithium salt, and could be beneficial to stabilise the interphase between cathode and electrolyte [57]. Similarly, for the electrodes subjected to multiple cycles in PIM, three peaks can be identified in the F1s spectra again, which are mainly assigned to the same species (the peak at 687.8 eV could also possibly contain some contribution from electrolyte decomposition products). When considering the formation of the CEI layer, it is interesting to note that the presence of another crucial inorganic solid component (Li-N species) was also observed in the N1s spectra (398.9 eV). This ion-conductive compound could also contribute to build a more robust CEI layer and enhance the Li^+ transport between the electrode/electrolyte interface [51]. With regard to the symmetric cation (P_{4444}^+), the only peak detected in the P2p spectra ($P2p_{1/2}$ at 133.3 eV, $P2p_{3/2}$ at 132.5 eV) is related to a phosphate group [20], which is attributed to the decomposition of P_{4444}^+ at the high voltage. Such phosphates would contribute to the enhanced thermal stability of the CEI layer, which is usually achieved by the introduction of certain electrolyte additives to build a more stable CEI layer [58], especially in Li- rich layered oxides [59,60]. Furthermore, the presence of phosphates may be beneficial to eliminate reactive oxygen radicals, that might be generated during the charge process in Li- rich cathodes [44]. Therefore, the superior performance of LRNM in PIM compared to LP30 may be due to the reduced detrimental effect of HF formation (in significantly lower amounts) and a more stable CEI layer derived from partial PIM decomposition during the charge/discharge process. Consequently, PIM exhibits a notable advantage over conventional organic carbonate-based electrolytes for lithium-rich cathode materials.

4. Conclusions

In summary, the novel high-voltage electrolyte based on the phosphonium $P_{4444}IM_{14}$ ionic liquid (PIM) displays exceptional electrochemical stability which has yet to be evidenced up to now in the literature. PIM also possesses excellent thermal stability of up to more than 200°C. When used as electrolyte solvent for high-voltage, lithium-metal cells employing LRNM cathodes, a remarkable electrochemical performance with respect to discharge capacity and initial Coulombic efficiency can be achieved. The excellent performance of PIM, which is superior to standard organic carbonate-based electrolytes, is associated with the peculiar chemistry of $P_{4444}IM_{14}$ with a stable phosphonium cation in combination with a highly asymmetric, but stable anion. The present work outlines a new strategy for developing enhanced electrolytes harnessing the full potential of high-voltage cathode materials for next-generation, high-energy lithium-metal battery systems.

Declaration of competing interest

The authors declare that they have no known competing financial interests or personal relationships that could have appeared to influence the work reported in this paper.

CRediT authorship contribution statement

Fanglin Wu: Investigation, Data curation, Writing – original draft. **Annika Regitta Schür:** Investigation. **Guk-Tae Kim:** Methodology, Supervision. **Xu Dong:** Investigation. **Matthias Kuenzel:** Writing – review & editing. **Thomas Diemant:** Investigation. **Gina D'Orsi:** Investigation. **Elisabetta Simonetti:** Investigation. **Massimo De Francesco:** Investigation. **Mariangela Bellusci:** Investigation. **Giovanni Battista Appetecchi:** Conceptualization, Methodology, Validation, Data curation, Writing – review & editing, Supervision, Funding acquisition. **Stefano Passerini:** Writing – review & editing, Supervision, Funding acquisition.

Acknowledgments

This project has received funding from the European Union's Horizon 2020 research and innovation programme under grant agreement No 814464 (Si-Drive project). The authors would also acknowledge financial support from the German Federal Ministry of Education and Research (BMBF) within the LILLINT (03XP0225D) project. F.W. gratefully acknowledges the financial support from the Chinese Scholarship Council (CSC). The financial support of the Helmholtz Association is also acknowledged.

Supplementary materials

Supplementary material associated with this article can be found, in the online version, at doi:10.1016/j.ensm.2021.08.030.

References

[1] R. Schmuch, R. Wagner, G. Hörpel, T. Placke, M. Winter, Nature Energy 3 (2018) 267–278.
[2] C. Niu, H. Lee, S. Chen, Q. Li, J. Du, W. Xu, J.-G. Zhang, M.S. Whittingham, J. Xiao, J. Liu, Nature Energy 4 (2019) 551–559.
[3] J. Qian, W.A. Henderson, W. Xu, P. Bhattacharya, M. Engelhard, O. Borodin, J.G. Zhang, Nat. Commun. 6 (2015) 6362.
[4] M.S. Ding, S.L. Koch, S. Passerini, Electrochim. Acta 240 (2017) 408–414.
[5] M.A. Navarra, MRS Bull. 38 (2013) 548–553.
[6] G.A. Elia, U. Ulissi, S. Jeong, S. Passerini, J. Hassoun, Energy Environ. Sci. 9 (2016) 3210–3220.
[7] G.A. Elia, U. Ulissi, F. Mueller, J. Reiter, N. Tsiouvaras, Y.K. Sun, B. Scrosati, S. Passerini, J. Hassoun, Chemistry 22 (2016) 6808–6814.
[8] L. Dong, F. Liang, D. Wang, C. Zhu, J. Liu, D. Gui, C. Li, Electrochim. Acta 270 (2018) 426–433.
[9] X. Wu, X. Li, Z. Wang, H. Guo, P. Yue, Ionics 19 (2012) 379–383.
[10] E. Simonetti, M. De Francesco, M. Bellusci, G.T. Kim, F. Wu, S. Passerini, G.B. Appetecchi, ChemSusChem 12 (2019) 4946–4952.
[11] T. Evans, D.M. Piper, H. Sun, T. Porcelli, S.C. Kim, S.S. Han, Y.S. Choi, C. Tian, D. Nordlund, M.M. Doeff, C. Ban, S.J. Cho, K.H. Oh, S.H. Lee, Adv. Mater. (2017) 29.
[12] J. Li, S. Jeong, R. Kloepsch, M. Winter, S. Passerini, J. Power Sources 239 (2013) 490–495.
[13] A. Heist, S. Hafner, S.-H. Lee, J. Electrochem. Soc. 166 (2019) A873–A879.
[14] S. Jeremias, M. Carewska, L. Conte, S. Passerini, G.B. Appetecchi, RSC Adv. 3 (2013) 17755.
[15] R.E. Del Sesto, C. Corley, A. Robertson, J.S. Wilkes, J. Organomet. Chem. 690 (2005) 2536–2542.
[16] G.M. Girard, M. Hilder, H. Zhu, D. Nucciarone, K. Whitbread, S. Zavorine, M. Moser, M. Forsyth, D.R. MacFarlane, P.C. Howlett, Phys. Chem. Chem. Phys.: PCCP 17 (2015) 8706–8713.
[17] X. Lin, R. Kavian, Y. Lu, Q. Hu, Y. Shao-Horn, M.W. Grinstaff, Chem. Sci. 6 (2015) 6601–6606.
[18] F. Chen, R. Kerr, M. Forsyth, J. Chem. Phys. 148 (2018) 193813.
[19] G.M.A. Girard, M. Hilder, D. Nucciarone, K. Whitbread, S. Zavorine, M. Moser, M. Forsyth, D.R. MacFarlane, P.C. Howlett, J. Phys. Chem. C 121 (2017) 21087–21095.
[20] G.M.A. Girard, M. Hilder, N. Dupre, D. Guyomard, D. Nucciarone, K. Whitbread, S. Zavorine, M. Moser, M. Forsyth, D.R. MacFarlane, P.C. Howlett, ACS Appl. Mater. Interfaces 10 (2018) 6719–6729.
[21] J. Kalhoff, G.G. Eshetu, D. Bresser, S. Passerini, ChemSusChem 8 (2015) 2154–2175.
[22] K. Tsunashima, Y. Sakai, M. Matsumiya, Electrochem. Commun. 39 (2014) 30–33.
[23] F. Wu, G.T. Kim, M. Kuenzel, H. Zhang, J. Asenbauer, D. Geiger, U. Kaiser, S. Passerini, Adv. Energy Mater. 9 (2019) 1902445.
[24] M. Kuenzel, H. Choi, F. Wu, A. Kazzazi, P. Axmann, M. Wohlfahrt-Mehrens, D. Bresser, S. Passerini, ChemSusChem 13 (2020) 2650–2660.
[25] W. Li, B. Song, A. Manthiram, Chem. Soc. Rev. 46 (2017) 3006–3059.

[26] W. Liu, P. Oh, X. Liu, S. Myeong, W. Cho, J. Cho, Adv. Energy Mater. 5 (2015) 1500274.
[27] M. Montanino, F. Alessandrini, S. Passerini, G.B. Appetecchi, Electrochim. Acta 96 (2013) 124–133.
[28] O. Palumbo, F. Trequattrini, G. Appetecchi, A. Paolone, Challenges 8 (2017) 7.
[29] G.B. Appetecchi, M. Montanino, M. Carewska, M. Moreno, F. Alessandrini, S. Passerini, Electrochim. Acta 56 (2011) 1300–1307.
[30] E. Paillard, Q. Zhou, W.A. Henderson, G.B. Appetecchi, M. Montanino, S. Passerini, J. Electrochem. Soc. 156 (2009) A891.
[31] G.B. Appetecchi, M. Montanino, S. Passerini, in: Ionic Liquids: Science and Applications, 1117, 2012, p. 67. A. E. Visser, N. J. Bridges and R. D. Rogers.
[32] M. Montanino, M. Carewska, F. Alessandrini, S. Passerini, G.B. Appetecchi, Electrochim. Acta 57 (2011) 153–159.
[33] W. Xu, E.I. Cooper, C.A. Angell, J. Phys. Chem. B 107 (2003) 6170–6178.
[34] M. Montanino, M. Moreno, F. Alessandrini, G.B. Appetecchi, S. Passerini, Q. Zhou, W.A. Henderson, Electrochim. Acta 60 (2012) 163–169.
[35] K. Tsunashima, M. Sugiya, Electrochem. Commun. 9 (2007) 2353–2358.
[36] K.J. Fraser, D.R. MacFarla, Aust. J. Chem. 62 (2009) 309–321.
[37] P.J. Griffin, A.P. Holt, K. Tsunashima, J.R. Sangoro, F. Kremer, A.P. Sokolov, J. Chem. Phys. 142 (2015) 084501.
[38] G.B. Appetecchi, Phys. Sci. Rev. (2019) 4.
[39] S. Brutti, E. Simonetti, M. De Francesco, A. Sarra, A. Paolone, O. Palumbo, S. Fantini, R. Lin, A. Falgayrat, H. Choi, M. Kuenzel, S. Passerini, G.B. Appetecchi, J. Power Sources 479 (2020) 228791.
[40] E.S.M. Moreno, G.B. Appetecchi, M. Carewska, M. Montanino, G.-T. Kim, N. Loeffler, S. Passerinid, J. Electrochem. Soc. 164 (2017) A6026–A6031.
[41] X. Qi, B. Blizanac, A. DuPasquier, P. Meister, T. Placke, M. Oljaca, J. Li, M. Winter, Phys. Chem. Chem. Phys.: PCCP 16 (2014) 25306–25313.
[42] K. Tsunashima, A. Kawabata, M. Matsumiya, S. Kodama, R. Enomoto, M. Sugiya, Y. Kunugi, Electrochem. Commun. 13 (2011) 178–181.
[43] H.-J. Liaw, C.-C. Chen, Y.-C. Chen, J.-R. Chen, S.-K. Huang, S.-N. Liu, Green Chem. 14 (2012) 2001.
[44] E.M. Erickson, F. Schipper, T.R. Penki, J.-Y. Shin, C. Erk, F.-F. Chesneau, B. Markovsky, D. Aurbach, J. Electrochem. Soc. 164 (2017) A6341–A6348.
[45] M. Wang, Y. Tang, Adv. Energy Mater. 8 (2018) 1703320.
[46] J. Pires, L. Timperman, A. Castets, J.S. Peña, E. Dumont, S. Levasseur, R. Dedryvère, C. Tessier, M. Anouti, RSC Adv. 5 (2015) 42088–42094.
[47] K. Xu, Chem. Rev. 104 (2004) 4303–4417.
[48] R.-S. Kühnel, M. Lübke, M. Winter, S. Passerini, A. Balducci, J. Power Sources 214 (2012) 178–184.
[49] F. Wu, G.T. Kim, T. Diemant, M. Kuenzel, A.R. Schür, X. Gao, B. Qin, D. Alwast, Z. Jusys, R.J. Behm, D. Geiger, U. Kaiser, S. Passerini, Adv. Energy Mater. 10 (2020) 2001830.
[50] J.U. Choi, N. Voronina, Y.K. Sun, S.T. Myung, Adv. Energy Mater. (2020) 2002027.
[51] W. Zhao, J. Zheng, L. Zou, H. Jia, B. Liu, H. Wang, M.H. Engelhard, C. Wang, W. Xu, Y. Yang, J.-G. Zhang, Adv. Energy Mater. 8 (2018) 1800297.
[52] V. Shutthanandan, M. Nandasiri, J. Zheng, M.H. Engelhard, W. Xu, S. Thevuthasan, V. Murugesan, J. Electron Spectrosc. Relat. Phenom. 231 (2019) 2–10.
[53] G.G. Eshetu, T. Diemant, S. Grugeon, R.J. Behm, S. Laruelle, M. Armand, S. Passerini, ACS Appl. Mater. Interfaces 8 (2016) 16087–16100.
[54] M. Stich, M. Göttlinger, M. Kurniawan, U. Schmidt, A. Bund, J. Phys. Chem. C 122 (2018) 8836–8842.
[55] J. Zheng, P. Yan, J. Zhang, M.H. Engelhard, Z. Zhu, B.J. Polzin, S. Trask, J. Xiao, C. Wang, J. Zhang, Nano Res. 10 (2017) 4221–4231.
[56] Y. Ji, P. Zhang, M. Lin, W. Zhao, Z. Zhang, Y. Zhao, Y. Yang, J. Power Sources 359 (2017) 391–399.
[57] B. Qin, S. Jeong, H. Zhang, U. Ulissi, D. Vieira Carvalho, A. Varzi, S. Passerini, ChemSusChem 12 (2019) 208–212.
[58] H. Ota, A. Kominato, W.-J. Chun, E. Yasukawa, S. Kasuya, J. Power Sources 119-121 (2003) 393–398.
[59] Z.Z. Shi Tan, Yixiao Li, Yun Li, Jianming Zheng, Zhibin Zhou, Yong Yang, J. Electrochem. Soc. 160 (2013) A285–A292.
[60] J. Zhang, J. Wang, J. Yang, Y. NuLi, Electrochim. Acta 117 (2014) 99–104.